

# Extrinsic higher-order topological corner states in AB-stacked transition-metal dichalcogenides

Jiang Yao<sup>1</sup> and Linhu Li<sup>1,\*</sup>

<sup>1</sup>*Guangdong Provincial Key Laboratory of Quantum Metrology and Sensing & School of Physics and Astronomy, Sun Yat-Sen University (Zhuhai Campus), Zhuhai 519082, China*

(Dated: August 14, 2023)

Higher-order topological insulators (HOTIs) are a novel type of topological phases which supports  $d$ -dimensional topological boundary states in  $D$ -dimensional systems with  $D-d > 1$ . In this work, we theoretically predict that interlayer couplings in AB-stacked bilayer transition-metal dichalcogenides (TMDs) lead to the emergence of extrinsic second-order topological phases, where corner states are induced by the band inversion of zigzag edge bands. We find that the systems feature a quantized multiband Berry phase defined for a zigzag nanoribbon geometry, unveiling the nontrivial topological properties of its two zigzag edges. With detailed investigation into the bilayer TMDs under different geometries, we find two types of boundary-obstructed corner states arising from different corner terminations of either the same type of or heterogeneous zigzag edges. The topological nature of these corner states and their degeneracy is further analyzed with both the crystalline symmetries of different geometries, and a topological phase transition of the Berry phase induced by a layer-dependent onsite energy.

## I. INTRODUCTION

Topological insulators are materials that exhibit robust boundary states, protected by a band gap and distinctive topological properties of their bulk states<sup>1,2</sup>. Their topological features can be classified into different “orders”, namely, a  $n$ th-order topological insulators in  $d$ -dimension ( $dD$ ) host topological boundary states in its  $(d-n)D$  boundaries. Topological insulators with their orders of topology higher than 1 are known as the higher-order topological insulators (HOTIs)<sup>3,4</sup>, whose realization has been proposed and implemented in both materials<sup>5-9</sup> and quantum simulation setups such as two-dimensional dielectric photonic crystals<sup>10</sup>, acoustic crystals<sup>11-14</sup> and two-dimensional continuous elastic system<sup>15</sup>.

Over the past decade, exploring novel topological phases such as HOTIs in natural electronic systems has been one of the most active research topics in condensed matter physics and material science<sup>16-18</sup>. Among the variety of natural materials, semiconducting 2D transition metal dichalcogenides (TMDs) possess a large bulk gap and in-gap 1D boundary states<sup>19</sup>, thus they provide an ideal platform for investigating various boundary phenomena. In particular, HOTI phases have been demonstrated to arise from double band inversion of surface states in the  $\beta$ - and  $\gamma$ - phases of TMDs<sup>20</sup>, or from staggered coupling amplitudes between different orbitals and  $C_3$  rotation symmetry in TMD monolayers<sup>21-23</sup>, whose connection to the orbital Hall effect has been recently unveiled<sup>24</sup>.

In this paper, we predict the presence of higher-order topological corner states in AB-stacked bilayer TMDs, based on a three-band tight-binding model describing the low-energy and edge-state physics in monolayers of group-VIB TMDs<sup>25</sup>. Recently, such structures have been shown to support different types of first-order topological phases<sup>26</sup>. Conventionally, corner states are expected to

be more accessible in TMDs with armchair boundaries, which possess a large energy gap between the 1D boundary states, whilst zigzag boundary states are gapless and may overwhelm possible corner states<sup>19,21,22</sup>. However, we find that interlayer couplings can induce a zigzag-boundary band inversion for bilayer TMDs, and generates corner states corresponding to the boundary obstructed topological phases with “extrinsic” higher-order topology, without relying on crystalline symmetries of the system<sup>27-36</sup>. Unlike a single monolayer, AB-stacking structure allows for two types of spatially symmetric zigzag boundaries, formed by boundaries of the two layers with different atoms. Interestingly, we find that different terminations between them give rise to two classes of corner states, where only one of them shows a direct correspondence to boundary-gap closing and a topological transition characterized by a Berry phase. These rich phenomena are exhaustively investigated with triangular, hexagonal, and parallelogram geometries, which support either one or both types of zigzag boundaries and thus different corner terminations.

The rest of this paper is organized as follows. In Sec. II, we introduce the three-orbital tight-binding model we use to describe AB-stacked bilayer TMDs, including their nontrivial topology characterized by a Berry phase, and crystalline symmetries that assist our analysis of corner states under different geometries. In Sec. III, we study the emergence of corner states and their behaviors during topological phase transitions of the Berry phase, in triangular, hexagonal, and parallelogram lattices respectively, and analyze their spatial configurations with the help of presence and absence of different crystalline symmetries. A summary and some discussion of our results are given in Sec. IV.

## II. MODEL

### A. Lattice structure and Hamiltonian

The systems we consider are AB-stacked bilayer TMDs, commonly referred as  $\text{MX}_2$  with M and X denoting atoms of transition metals and chalcogens respectively, with a honeycomb-like structure as sketched in Fig. 1(a). To analyze the edge and corner physics we concern, we adopt a three-orbital model for each layer<sup>25</sup>, constructed using only the  $d_{z^2}$ ,  $d_{xy}$ , and  $d_{x^2-y^2}$  orbitals of M atoms, which gives a reasonable description of zigzag edge states of these materials, and has been applied to investigate various edge phenomena therein<sup>24,37-39</sup>. The tight-binding Hamiltonian can be written as

$$\hat{H} = \hat{H}_{1\text{st}} + \hat{H}_{2\text{nd}} + \hat{H}_{\text{int}} + \frac{\mu}{2}(\hat{N}_1 - \hat{N}_2), \quad (1)$$

with  $\hat{H}_{1\text{st}}$  ( $\hat{H}_{2\text{nd}}$ ) the monolayer Hamiltonian for the top (bottom) layer,  $\hat{H}_{\text{int}}$  the interlayer couplings, and  $\hat{N}_{1,2}$  the total electron number operator. The last term of  $\mu$  describes the difference of on-site energy for the two layers, which may be induced by external electric fields applied perpendicular to the layers<sup>40,41</sup>. Note that a nonzero  $\mu$  is not essential to induce corner states in our systems. However, it can lead to a topological phase transition that changes the number of corner states, as demonstrated in later sections.

Explicitly, the first two Hamiltonian operators are given by

$$\hat{H}_{1\text{st}} = \sum_{i,\mathbf{R}} \sum_{\alpha,\alpha'} \hat{a}_{i,\alpha}^\dagger t_{\mathbf{R},\alpha,\alpha'} \hat{a}_{i+\mathbf{R},\alpha'} + \sum_{i,\alpha} \hat{a}_{i,\alpha}^\dagger \epsilon_\alpha \hat{a}_{i,\alpha}, \quad (2)$$

$$\hat{H}_{2\text{nd}} = \sum_{i,\mathbf{R}} \sum_{\alpha,\alpha'} \hat{b}_{i,\alpha}^\dagger t_{\mathbf{R},\alpha,\alpha'} \hat{b}_{i+\mathbf{R},\alpha'} + \sum_{i,\alpha} \hat{b}_{i,\alpha}^\dagger \epsilon_\alpha \hat{b}_{i,\alpha}, \quad (3)$$

Where  $\hat{a}_{i,\alpha}^\dagger$  ( $\hat{b}_{i,\alpha}^\dagger$ ) creates an electron at lattice site  $i$  and orbital  $\alpha$  in the top (bottom) layer,  $\mathbf{R}$  is one of the six vectors connecting nearest-neighbor M atoms with  $t_{\mathbf{R},\alpha,\alpha'}$  being its corresponding hopping strength [see Fig. 1(a) and Table. I], and  $\epsilon_\alpha$  are on-site energies corresponding to different orbitals,

The third term  $\hat{H}_{\text{int}}$  in Eq.1 is the interlayer hopping. Using Slater-Koster table<sup>42</sup>,  $\hat{H}_{\text{int}}$  reads

$$\begin{aligned} \hat{H}_{\text{int}} = & \hat{a}_{i,d_{z^2}}^\dagger V_{dd\sigma} \hat{b}_{i,d_{z^2}} + \hat{a}_{i,d_{xy}}^\dagger V_{dd\delta} \hat{b}_{i,d_{xy}} \\ & + \hat{a}_{i,d_{x^2-y^2}}^\dagger V_{dd\delta} \hat{b}_{i,d_{x^2-y^2}} + H.c., \end{aligned} \quad (4)$$

Where  $V_{dd\sigma}$  and  $V_{dd\delta}$  are two types of overlap integrals of different d-d orbitals, and  $V_{dd\sigma}$  is generally much larger than  $V_{dd\delta}$  for a relatively large distance between M atoms<sup>43,44</sup>. In the following discussion, we shall assume

$$V_{dd\sigma} = \nu, \quad V_{dd\delta} = 0.3\nu, \quad (5)$$

and use the tight-binding parameters for  $\text{MoS}_2$  given in Ref.<sup>25</sup> ( $\epsilon_{d_{z^2}} = 1.046$  eV,  $\epsilon_{d_{xy}} = \epsilon_{d_{x^2-y^2}} = 2.104$  eV, ; see Table I for other parameters), unless otherwise specified.

### B. Zigzag edge states and edge-band inversion in a nanoribbon structure

To reveal the topological nature that gives rise to higher-order corner states, we take a look at the system with a zigzag nanoribbon structure along  $x$  direction. When  $\mu = \nu = 0$ , our model reduces to two identical monolayers of TMDs, where edge bands of different zigzag edge states (namely, M-edge and X-edge) of the two layer cross each other in their eigenenergies. The AB-stacked structure allows for a mixture of the two branches of edge states on the same edge of the bilayer TMD, denoted as M-X or X-M edge according to the boundary atoms of the two layers [see Fig. 1(a)]. Thus, with a nonzero  $\nu$  that couples M- and X-edges of different layers, an edge-band inversion occurs and opens a boundary gap between these edge states, as shown in Fig. 1(b) and (c). Note that these edge states are two-fold degenerate when  $\mu = 0$ , due to an inversion symmetry between M-X and X-M edges. With a nonzero  $\mu$ , the degeneracy is lifted, and one pair of edge states is separated in energy (the one at X-M edge for a positive  $\mu$ ), resulting in a reversed process of band inversion and thus a topological phase transition, as shown in Fig. 2. These different topological phases can be further characterized by a multi-band Berry phase  $\gamma$ , defined as

$$\gamma = -i \sum_l \log \det U(k_l), \quad (6)$$

where  $U_{mn}(k_l) = \langle \psi_m(k_l) | \psi_n(k_{l+1}) \rangle$  is the  $(m, n)$  element of the link matrix  $U(k_l)$ ,  $|\psi_m(k_l)\rangle$  is the Bloch wavefunction of the  $m$ -th band at the discrete crystal momentum  $k_l$ , and  $m, n \in [1, N_{\text{occ}}]$  with  $N_{\text{occ}}$  the number of occupied bands (all bands below the edge-gap in our case, see Fig. 2).

Numerically, we find that  $\gamma = 0$  for small  $\mu$  with band inversion for both M-X and X-M edge states [Fig. 2(a)], as they possess opposite topological charges characterized by single-band Berry phases of  $\pm\pi$  respectively (see Appendix A). Nonetheless, corner states may still emerge under the full OBCs with different geometries, as demonstrated in later sections. This is because the 1D edges are spatially separated by the bulk, therefore their opposite topological charges cannot annihilate each other. On the other hand, increasing  $\mu$  will lead to a topological phase transition and trivialize one pair of edge states, resulting in a  $\pi$  Berry phase contributed solely by the other pair with edge-band inversion, as illustrated in Fig. 2(c). Following this analysis, the topological phase transition shall occur when the amplitude of  $\mu$  matches the energy difference between the maximal value of M-edge band and minimal value of X-edge band [see Fig. 1(b)],  $\mu \approx |E_M - E_X| \approx 0.67$  eV, which is verified in the explicit examples discussed in later sections. A topological phase diagram regarding different values of  $\nu$  and  $\mu$  is displayed in Fig. 2(d), which shows that the strength of interlayer coupling  $\nu$  does not affect much the Berry phase or the topological transition induced by  $\mu$ . In other words, the

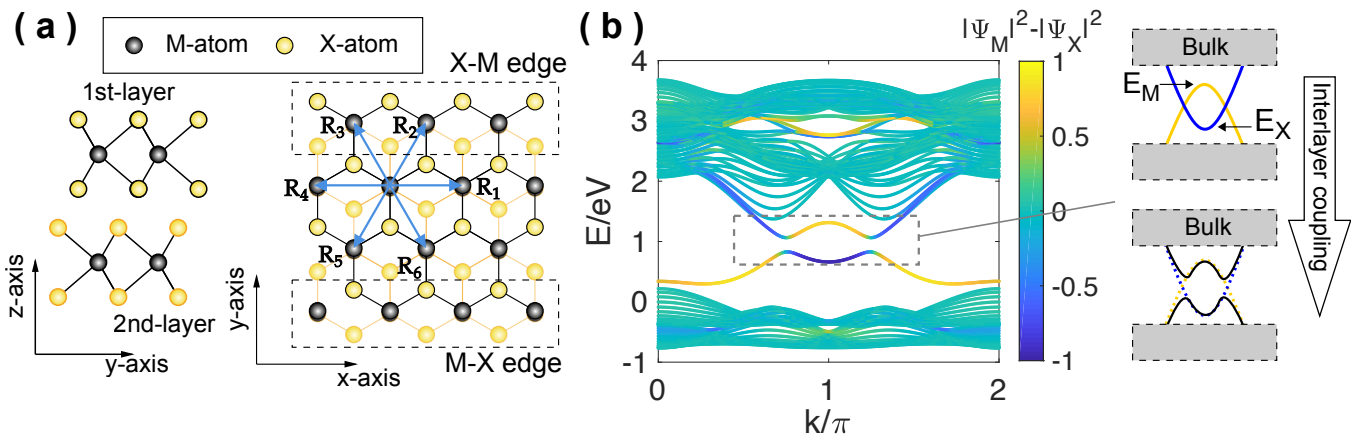


FIG. 1. Lattice structure and energy spectrum of AB-stacked bilayer TMDs. (a) Side view and top view of the model, with  $\mathbf{R}_1$  to  $\mathbf{R}_6$  indicating the nearest neighbors. Dashed boxes show different zigzag edges in AB-stacked TMDs. (b) Energy spectrum of a zigzag nanoribbon, with  $\nu = 0.3$  eV and  $\mu = 0$ . Eigenstates are marked by different colors according to the quantity  $|\Psi_M|^2 - |\Psi_X|^2$ , where  $|\Psi_M|^2$  ( $|\Psi_X|^2$ ) is the sum distribution at M edges (X edges) for each eigenstate. Namely,  $|\Psi_M|^2 - |\Psi_X|^2 \approx 1$  for M edge states, and  $\approx -1$  for X edge states. Right panel in (b) sketches the band inversion mechanism of zigzag edge bands.  $E_M$  and  $E_X$  are the maximal value of M-edge band and the minimal value of X-edge band, respectively. For  $\text{MoS}_2$ ,  $E_M \approx 1.32$  eV and  $E_X \approx 0.65$  eV.

TABLE I. Hopping amplitudes  $t_{\mathbf{R},\alpha,\alpha'}$  for TMDs<sup>25,37</sup>. Different rows show hoppings between different orbitals, and different columns are for different spatial hopping vectors  $\mathbf{R}$  for the top layer in Fig.1. For the bottom layer,  $\mathbf{R}_1$ ,  $\mathbf{R}_2$ , and  $\mathbf{R}_3$  are exchanged with  $\mathbf{R}_4$ ,  $\mathbf{R}_5$ , and  $\mathbf{R}_6$ , respectively. For  $\text{MoS}_2$ , the parameters are approximately given by  $t_0 = -0.184$ ,  $t_1 = 0.401$ ,  $t_2 = 0.507$ ,  $t_{11} = 0.218$ ,  $t_{12} = 0.338$ ,  $t_{22} = 0.057$  (in eV)<sup>37</sup>.

$\alpha-\alpha'$	$\mathbf{R}_1$	$\mathbf{R}_2$	$\mathbf{R}_3$	$\mathbf{R}_4$	$\mathbf{R}_5$	$\mathbf{R}_6$
$d_{z^2}-d_{z^2}$	$t_0$	$t_0$	$t_0$	$t_0$	$t_0$	$t_0$
$d_{xy}-d_{xy}$	$t_{11}$	$\frac{t_{11}+3t_{22}}{4}$	$\frac{t_{11}+3t_{22}}{4}$	$t_{11}$	$\frac{t_{11}+3t_{22}}{4}$	$\frac{t_{11}+3t_{22}}{4}$
$d_{z^2}-d_{xy}$	$t_1$	$\frac{t_1+\sqrt{3}t_2}{2}$	$-\frac{t_1+\sqrt{3}t_2}{2}$	$-t_1$	$-\frac{t_1+\sqrt{3}t_2}{2}$	$\frac{t_1-\sqrt{3}t_2}{2}$
$d_{z^2}-d_{x^2-y^2}$	$t_2$	$-\frac{t_2-\sqrt{3}t_1}{2}$	$-\frac{t_2-\sqrt{3}t_1}{2}$	$t_2$	$-\frac{t_2+\sqrt{3}t_1}{2}$	$-\frac{t_2+\sqrt{3}t_1}{2}$
$d_{xy}-d_{x^2-y^2}$	$t_{12}$	$\frac{\sqrt{3}(t_{11}-t_{22})}{4} - t_{12}$	$\frac{\sqrt{3}(t_{22}-t_{11})}{4} + t_{12}$	$-t_{12}$	$\frac{\sqrt{3}(t_{11}-t_{22})}{4} + t_{12}$	$\frac{\sqrt{3}(t_{22}-t_{11})}{4} - t_{12}$

nontrivial topology and its corresponding higher-order corner states are not sensitive to the exact value of interlayer couplings, and thus can be expected to manifest in a more realistic parameter regime [compared with our assumption in Eq. (5)] of TMD materials.

### C. Crystalline symmetries of the AB-stacked bilayer TMDs

Although no essential to the extrinsic higher-order corner states, the lattice structure of TMDs naturally hosts several crystal symmetries, which are useful in our analysis of corner states under different geometries. In particular, The space symmetry group of monolayer TMDs is the  $D_{3h}$  point group, containing symmetry operators  $\{\hat{E}, \hat{C}_3, \hat{C}_3^2, \hat{M}_x, \hat{M}_1, \hat{M}_2\}$ , where  $\hat{E}$  is the identity operation,  $\hat{C}_3$  is the rotation by  $\frac{2\pi}{3}$  about the  $z$ -axis,  $\hat{M}_x$  is the mirror-reflection along  $x$ -axis, and  $\hat{M}_1$  and  $\hat{M}_2$  are obtained through rotating  $\hat{M}_x$  around the  $z$ -axis by  $\frac{2\pi}{3}$  and  $\frac{4\pi}{3}$ , respectively. In addition to these symmetries,

AB-stacked bilayer TMDs (without a boundary) further satisfy a 3D inversion symmetry described by the operator  $\hat{I} = \sigma_x \hat{R}$ , with  $\sigma_x$  exchanges the two layers, and  $\hat{R}$  the central rotation around  $z$ -axis with 180 degree. An extra interlayer-mirror symmetry along  $y$ -axis also emerges, described by the operator  $\hat{M}'_y = \hat{I} \hat{M}_x$ , which represents a combination of mirror-reflection along  $y$ -axis and exchanging the two layers. This symmetry is also equivalent to a  $C_2$  symmetry around  $x$  axis in 3D.

### III. CORNER STATES UNDER DIFFERENT GEOMETRIC STRUCTURES

As seen in Fig. 2, nontrivial topological properties in our model originate from an edge-band inversion, which shall lead to the emergence of boundary obstructed topological corner states in the edge-gap near  $E = 0.95$  eV [dash lines in Fig. 2] under the full OBCs. More intriguingly, these corner states may show distinguished behaviors depending on the geometry of a OBC lattice, since shearing the lattice along different directions will result

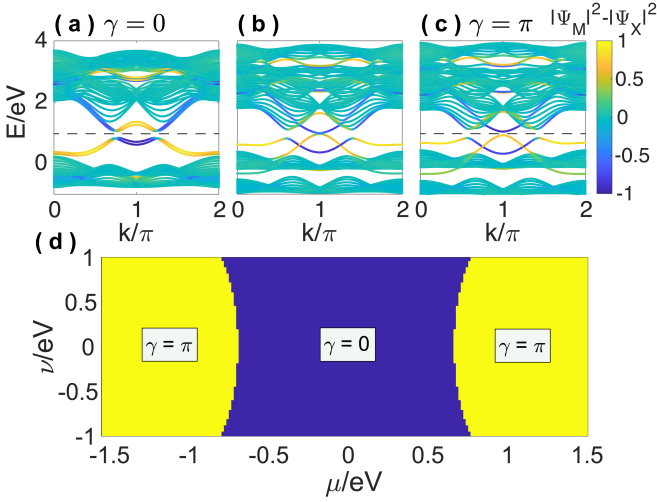


FIG. 2. Energy spectrum and a topological phase diagram of the bilayer TMDs in a nanoribbon structure, with  $\mu = 0.1$  eV, 0.68 eV, and 0.8 eV from (a) to (c) respectively, and the same colormap as in Fig. 1, indicating distribution of each eigenstate at M and X edges. With increasing  $\mu$ , a reversed process of band inversion occurs for one pair of edge states, which becomes topologically trivial after the transition at  $\mu \approx 0.67$  eV. In (a) and (c),  $\gamma$  is calculated for all eigenstates below the band gap (indicated by the dash lines). We find  $\gamma = 0$  in (a) as edge-band inversion occurs for both M-X and X-M edge states, which possess opposite single-band Berry phase (see Appendix A). In (c), we have  $\gamma = \pi$  since one pair of these edge states is trivialized after the topological phase transition. 1D edge states in (b) are gapless, and thus the Berry phase is ill-defined. Other parameters are the same as in Fig. 1. (d) A phase diagram determined by the value of  $\gamma$ .

in junctions either between heterogeneous M-X and X-M edges, or two edges of the same type.

### A. Triangular structure

We first consider AB-stacked bilayer TMDs with a triangular geometry, as shown in Figure.3(a). A triangular lattice has three equivalent boundaries of the same type, and here we take the case with M-X edges as an example. In addition, it satisfies the 3-fold rotation symmetry of  $\hat{C}_3$ , but not the inversion symmetry that exchanges the two layers. Thus the corner states in a triangular bilayer TMDs are expected to be symmetric between different corners, and asymmetric between the two layers.

In Fig. 3(b), we display our numerically results of eigenenergies for the triangular structure. Two groups of three-fold degenerate states with different energies are found within the edge-gap. Their distributions in real space are shown in Fig. 3(c) and (d), where each set of degenerate states distributes symmetrically on the three corners. On the other hand, the two sets of corner states exhibit different occupation on the two layers, as can be seen from the weight of occupation on each site of the

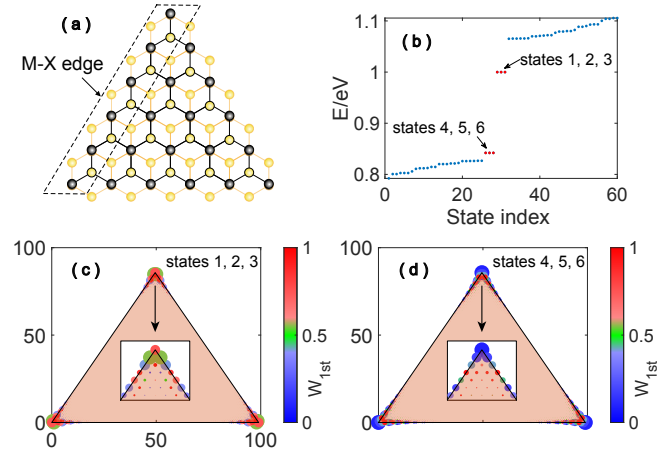


FIG. 3. Lattice structure and corner states in AB-stacked bilayer TMDs with a triangular structure. (a) Top view of the triangular lattice. (b) 60 Eigenenergies close to  $E = 0.95$  eV, with two sets of three-fold degenerate corner states (red) within the energy gap. (c) and (d) distribution of the two sets of three-fold degenerate corner states respectively. The size of each point is proportional to the summed distribution at each site  $i$ ,  $\rho_i = \sum_{\alpha,n} (|\psi_{i,\alpha,n}^{1st}|^2 + |\psi_{i,\alpha,n}^{2nd}|^2)$ , with  $\alpha$  denoting the three orbitals and  $n$  summing over the three states indicated in each panel. The colormap displays the value of  $W_i^{1st}$ , the weight of occupation on the first layer for each site. Namely,  $W_i^{1st} = 1$  (0) means that the states occupy only the first (second) layer on the lattice site indexed by  $i$ . The system's size is chosen to have 100 M atoms along each edge. Other parameters are  $\nu = 0.3$  eV and  $\mu = 0$ .

first layer,

$$W_i^{1st} = \sum_{n,\alpha} |\psi_{i,\alpha,n}^{1st}|^2 / \left( \sum_{n,\alpha} |\psi_{i,\alpha,n}^{1st}|^2 + \sum_{n,\alpha} |\psi_{i,\alpha,n}^{2nd}|^2 \right),$$

with  $\psi_{i,\alpha,n}^{1st(2nd)}$  the amplitude at the  $i$ th site of the 1st (2nd) layer of an eigenstate indexed by  $n$ , and the summation runs over all orbitals (indexed by  $\alpha$ ) for a set of degenerate corner states. Namely, states 1, 2, and 3 show a roughly balanced occupation on the two layers, and states 4, 5, and 6 mostly occupy the 2nd layer. Such asymmetric layer occupation for corner states at different eigenenergies reflects the absence of the inversion symmetry of  $\hat{I} = \sigma_x \hat{R}$  in the triangular lattice.

In Fig. 4, we illustrate the eigenenergies around the energy gap as a function of the layer-dependent on-site energy  $\mu$ , which are marked by different colors according to the inverse participation ratio (IPR) of their eigenstates, defined as

$$\text{IPR}(n) = \sum_i \left[ \sum_{\alpha} (|\psi_{i,\alpha,n}^{1st}|^2 + |\psi_{i,\alpha,n}^{2nd}|^2) \right]^2.$$

As can be seen from the figure, by turning on the layer-dependent on-site energy  $\mu$ , the energy gap closes between 1D edge states at  $\mu \approx -0.67$  eV, and corner

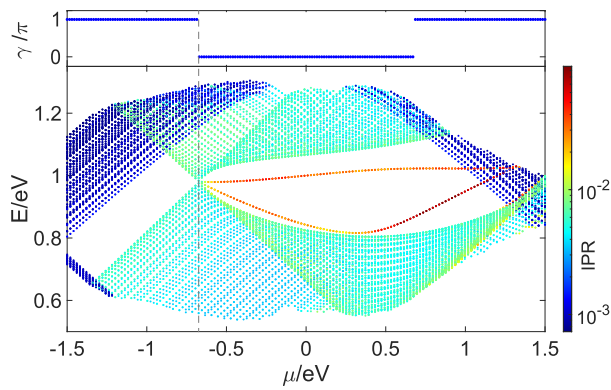


FIG. 4. Energy spectrum and Berry phase  $\gamma$  versus the layer-dependent on-site energy  $\mu$ , for the triangular lattice with  $\nu = 0.3$  eV. 200 energy points around  $E = 0.92$  eV are taken in our numerics. The side length of the lattice is chosen to be 70 M atoms.

states disappear when further decreasing the (negative) value of  $\mu$ . Such an observation matches a jump of the Berry phase  $\gamma$  from 0 to  $\pi$ , yet with two unconventional properties seemingly contradictory to conventional bulk-boundary correspondence of topological phases: (i) corner states emerge with a trivial Berry phase ( $\gamma = 0$ ), and disappear with a nontrivial one ( $\gamma = \pi$ ); and (ii) the same edge-gap closing does not occur at the other topological transition point of  $\mu \approx 0.67$  eV.

To understand these enigmatic behaviors, we note that the Berry phase is calculated under the nanoribbon geometry with both M-X and X-M edges, and the “trivial” phase with  $\gamma = 0$  is in fact nontrivial with single-band Berry phases of  $\pm\pi$  for the two edge bands, as discussed for Fig. 2 and in Appendix A. The triangular lattice we consider in Fig. 3 possesses only M-X edges, therefore it only inherits “half” of the topological properties of a nanoribbon geometry, which is trivialized when  $\mu \lesssim -0.67$  eV. Alternatively, a triangular lattice with X-M edges shall inherit the other “half” of the topological properties, possessing a spectrum symmetric to Fig. 4 regarding  $\mu = 0$ , with a topological phase transition at  $\mu \approx 0.67$  eV (no shown). As a side note, a large amplitude of  $\mu$  will shift different bulk bands of the two layers and mix them in energy, thus all corner states will eventually merge into the bulk bands even without a topological transition, as seen in Fig. 4 with  $\mu \gtrsim 1$  eV.

## B. Hexagonal structure

Next we consider a hexagonal structure of the AB-stacked bilayer TMDs, as sketched in Fig. 5(a). Unlike the triangular lattice, a hexagonal lattice has adjacent M-X and X-M edges, and satisfies both the inversion symmetry of  $\hat{I} = \sigma_x \hat{R}$  and the 3-fold rotation symmetry of  $\hat{C}_3$ . Consequently, corner states in the hexagonal lattice shall be six-fold degenerate, and distributes evenly on the two

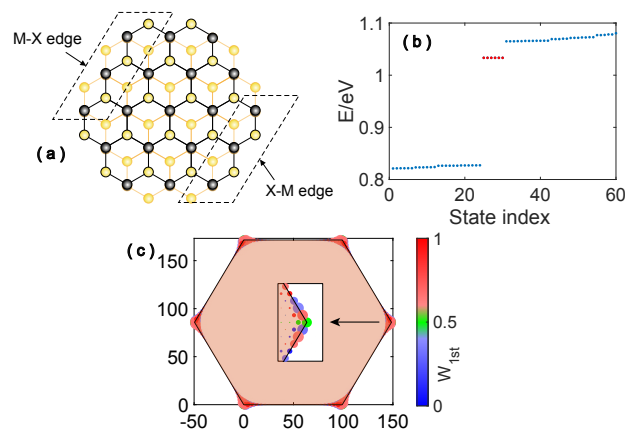


FIG. 5. Lattice structure and corner states in AB-stacked bilayer TMDs with a hexagonal structure. (a) Top view of the hexagonal lattice. (b) 60 Eigenenergies close to  $E = 0.95$  eV, with a set of six-fold degenerate corner states (red) within the energy gap. (c) distribution of the six degenerate corner states. The size of each point is proportional to the summed distribution  $\rho_i$  at site  $i$ , and the colormap displays the value of  $W_i^{1st}$ . The system’s size is chosen to have 100 M atoms along each edge. Other parameters are  $\nu = 0.3$  eV and  $\mu = 0$ .

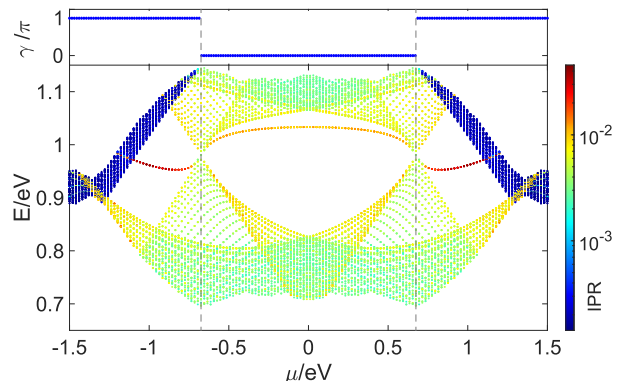


FIG. 6. Energy spectrum and Berry phase  $\gamma$  versus the layer-dependent on-site energy  $\mu$ , for the hexagonal lattice with  $\nu = 0.3$  eV. 200 energy points around  $E = 0.92$  eV are taken. The side length of the lattice is chosen to be 70 M atoms.

layers, as verified by our numerical results in Fig. 5(b) and (c).

Due to the different boundary terminations, corner states of the hexagonal lattice behave rather differently across the topological phase transition characterized by the Berry phase  $\gamma$ . As demonstrated in Fig. 6, the six-fold degenerate corner states survive in all the three parameter regions separated by the gap closing at  $\mu \approx \pm 0.67$  eV (except that they merge into bulk bands for  $\mu \gtrsim 1$  eV). This is because under a hexagonal geometry, each corner connects two distinct M-X and a X-M edges, and at least one of them is governed by nontrivial topology in the three parameter regions, resulting in a corner state at each of their joint corners.

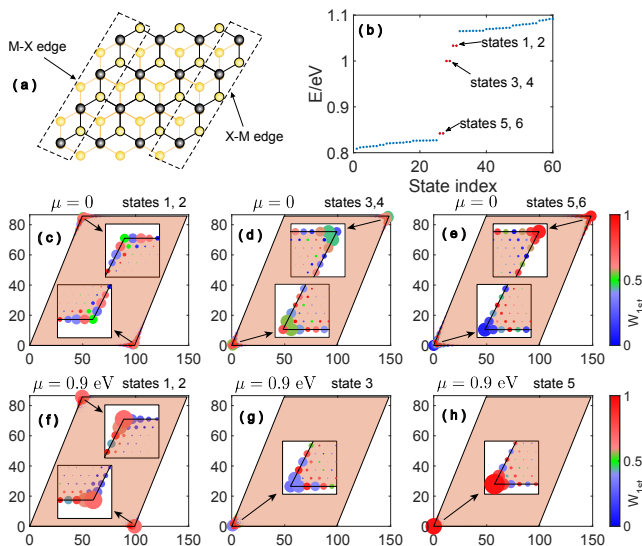


FIG. 7. Lattice structure and corner states in AB-stacked bilayer TMDs with a parallelogram structure. (a) Top view of the parallelogram lattice. (b) 60 Eigenenergies close to  $E = 0.95$  eV at  $\mu = 0$ , with three sets of two-fold degenerate corner states (red) within the energy gap. (c) to (e) distribution of the three sets of degenerate corner states respectively, with  $\mu = 0$ . The size of each point is proportional to the summed distribution  $\rho_i$  at site  $i$ , and the colormap displays the value of  $W_i^{1st}$ . The system's size is chosen to have  $N_x = N_y = 100$ , with  $N_x$  and  $N_y$  the number of M atoms along  $x$  and  $y$  directions respectively. (f) distribution of the degenerate corner states (1,2) with  $\mu = 0.9$ . (g) and (h) distribution of a single non-degenerate corner state with  $\mu = 0.9$ . These two states are marked as states 3 and 5, as they correspond to states (3,4) and (5,6) in a different topological phase with  $|\mu| \lesssim 0.67$  eV (see Fig. 8).  $\nu = 0.3$  eV is chosen for all panels.

### C. Parallelogram structure

From the aspect of boundary terminations, a parallelogram structure can be viewed as a mixture of triangular and hexagonal ones, as it support both types of corners connecting either the same or two different M-X and X-M edges, as sketched in Fig. 7(a). Consequently, corner states in a parallelogram lattice are expected to behave differently on different types of corners, which is also suggested by the lack of the  $C_3$  rotation symmetry in such a geometry.

The energy spectrum around the zigzag edge gap of AB-stacked bilayer TMDs in a parallelogram geometry is shown in Fig.7(b), where three sets of two-fold degenerate corner states are found inside the gap. Their distribution in real space is illustrated in Fig. 7(c) to (e), where one set of corner states (labeled as states 1 and 2) occupy the top-left and bottom-right corners, in analogous to the corner states in the hexagonal lattice; and the rest two (labeled as states 3 to 6) occupy the other two corners, in analogous to the corner states in the triangular lattice. Remarkably, due to the presence of the inversion symmetry ( $\hat{I} = \hat{R}\sigma_x$ ), each set of corner

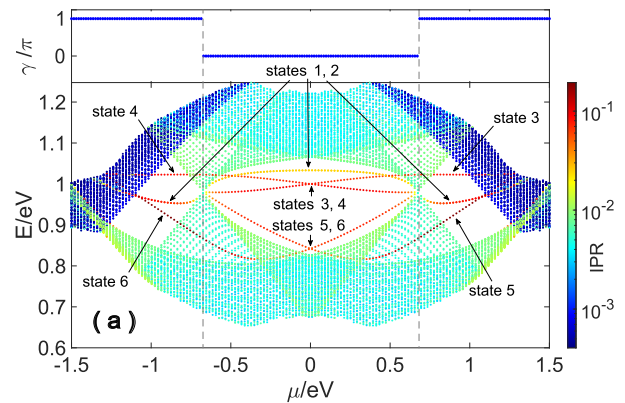


FIG. 8. Energy spectrum and Berry phase  $\gamma$  versus the layer-dependent on-site energy  $\mu$ , for the parallelogram lattice with  $\nu = 0.3$  eV. 200 energy points around  $E = 0.92$  eV are taken. The size of the lattice is chosen to be  $N_x = N_y = 70$ .

states now exhibits symmetric distribution on the two layers, in contrast to the case of the inversion-asymmetric triangular lattice.

Due to their different boundary terminations, these corner states behave rather differently upon turning on a nonzero  $\mu$ . As demonstrated in Fig. 8, the hexagonal-analogous corner states (1,2) remain degenerate and exist for all values of  $\mu$ , as they both originate from the same type of joint corners between M-X and X-M edges. In contrast, the two triangular-analogous corner states of a degenerate pair [(3, 4) or (5, 6)] originate from corners of different types of edges. That is, the bottom-left corner connect two M-X edges, and the top-right corner connect two X-M edges. As discussed previously for the triangular lattice, these two types of corners react to  $\mu$  differently (but symmetric about  $\mu = 0$ ), therefore their degeneracy is lifted by a nonzero  $\mu$ . Further increasing the amplitude of  $\mu$ , a topological phase transition occurs for M-X (X-M) edge when  $\mu < 0$  ( $\mu > 0$ ), and one corner state of each triangular-analogous pair disappear when  $|\mu| \gtrsim 0.67$  eV. The disappearing of two corner states at the same corner is in consistence with our results and analysis for the triangular lattice, which hosts three  $C_3$ -rotation-symmetric corners connecting the same type of edges.

### D. Symmetry-protected degeneracy of corner states

The above observations and analysis imply that in the parallelogram lattice, the two-fold degeneracy of triangular-analogous corner states is protected by the inversion symmetry, and the three-fold degeneracy of corner states in the triangular lattice is protected by the  $C_3$  rotation symmetry, rather than topological properties related to the Berry phase. Indeed, as shown in Fig. 9 that displays the energy spectrum versus  $\nu$  for the three dif-

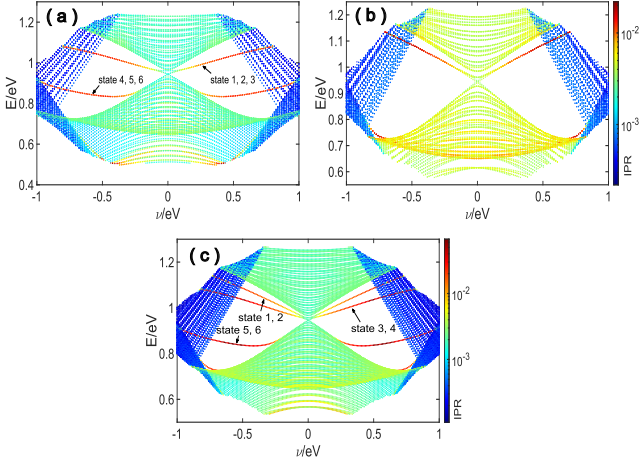


FIG. 9. Energy spectrum at  $\mu = 0$  versus interlayer hopping strength  $\nu$  for (a) the triangular structure with 200 points around 0.87 eV, (b) the hexagonal structure with 300 points around 0.9 eV, and (c) the parallelogram structure with 200 points around 0.9 eV.

ferent geometries, some of these corner states [states 4, 5, and 6 in (a) and states 5 and 6 in (c)] emerge from bulk bands when  $\nu$  exceeds a nonzero value, without involving gap closing between different bands. On the other hand, corner states in the hexagonal lattice, and those hexagonal-analogous ones in parallelogram lattice, arise from connection of heterogeneous edges and are always degenerate, manifesting the topological protection corresponding to the Berry phase.

#### IV. SUMMARY AND DISCUSSION

We have unveiled a class of extrinsic higher-order topological phases induced by interlayer couplings in AB-stacked bilayer TMDs, which host corner states insensitive to crystal symmetries of the materials. Explicitly, the zigzag edge states of these materials cross each other in their eigenenergy, thus a band inversion between them can be induced by nonzero interlayer couplings, leading to gapped edge bands and the emergence of in-gap corner states. With exhaustive investigation into the system with different triangular, hexagonal, and parallelogram geometries, we uncover two types of corner states corresponding to different corner terminations between the M-X and X-M zigzag edges for the bilayer structure. The topological nature of these corner states is justified by a multiband Berry phase defined for the system in a nanoribbon geometry, which reflects the overall topological properties of both types of zigzag edges. Topological phase transitions of the system induced by a on-site energy detuning  $\mu$  of the two layers are studied accordingly. We find that the M-X and X-M edges can be trivialized only for negative and positive  $\mu$  respectively, leading to distinct behaviors for the two types of corner states when

a topological phase transition occurs. Our results show that the higher-order corner states in bilayer TMDs are highly tunable due to the abundant bilayer structures and layer-dependent physical effects (such as a perpendicular electric field), and thus hold great promise for quantum applications.

Throughout our study, we have focused only on the zigzag edges, as they support gapless edge states and thus an edge band inversion can be induced by weak interlayer couplings. In Appendix B, we have further demonstrated numerical results of the AB-stacked bilayers TMDs in a square lattice, which support both zigzag and armchair edges. We find that corner states in square lattices may be attributed to either zigzag- or armchair-edge band inversion, yet the later occurs only with a relatively large interlayer hopping strength, due to the large armchair-edge band gap of monolayer TMDs.

#### V. ACKNOWLEDGEMENTS

This work is supported by the Guangdong Project (Grant No. 2021QN02X073).

#### Appendix A: Single-band Berry phases

In this appendix we discuss properties of single-band Berry phase  $\gamma_n$  for the zigzag edges of AB-stacked bilayer TMDs. It follows a similar definition as in Eq. (6) in the main text,

$$\gamma_n = -i \sum_l \log U_n(k_l), \quad (\text{A1})$$

with  $U_n(k_l) = \langle \psi_n(k_l) | \psi_n(k_{l+1}) \rangle$  and  $\psi_n(k_l)$  the Bloch wavefunction of the  $n$ -th band at the discrete crystal momentum  $k_l$ . Here we consider the two degenerate edge bands belong the energy gap in Fig. 1(b), labeled as  $\psi_{rMx}$  and  $\psi_{XM}$  respectively regarding their occupied edges. Due to the presence of inversion symmetry, these two edge bands are symmetric to each other between  $k$  and  $-k$ , i.e.

$$\hat{I}_y |\psi_{MX}(k)\rangle = |\psi_{XM}(-k)\rangle,$$

with  $\hat{I}_y = \hat{M}_y \sigma_x$  the inversion operation in  $y-z$  plane (the same as  $\hat{M}'_y$  discussed in Sec. II C). In addition, the model also satisfies the time reversal symmetry  $\hat{H}(k) = \hat{H}^*(-k)$ , or  $|\psi(k)\rangle = |\psi^*(-k)\rangle$  for eigenstates. Thus the link variable  $U_n(k)$  for these two bands satisfies

$$\begin{aligned} U_{MX}(k) &= \langle \psi_{MX}(k_l) | \psi_{MX}(k_{l+1}) \rangle \\ &= \langle \psi_{XM}(-k_l) | \psi_{XM}(-k_{l+1}) \rangle \\ &= \langle \psi_{XM}(k_l)^* | \psi_{XM}(k_{l+1})^* \rangle \\ &= \langle \psi_{XM}(k_l) | \psi_{XM}(k_{l+1}) \rangle^* \\ &= U_{XM}(k)^* \end{aligned} \quad (\text{A2})$$

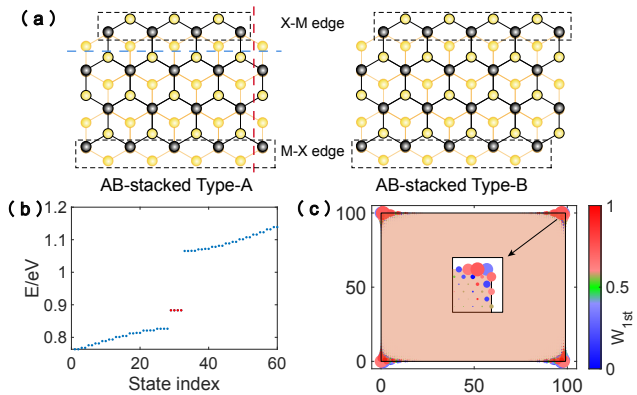


FIG. 10. Lattice structure and corner states in AB-stacked bilayer TMDs with square structures. (a) Top view of different types square structures. A type-B lattice can be obtained from a type-A one by shearing along the red dash line. Shearing along the blue dash line changes the parity of  $N_y$ . (b) 60 Eigenenergies close to  $E = 0.95$  eV at  $\mu = 0$  for the type-A square lattice with an odd  $N_y$ , with four degenerate corner states (red) within the energy gap. (c) distribution of the the degenerate corner states, where the size of each point is proportional to the summed distribution  $\rho_i$  at site  $i$ , and the colormap displays  $W_i^{1st}$ , the weight of the first-layer occupation on each site. The system's size is chosen to be  $N_x = 100$  and  $N_y = 101$ . Other parameters are  $\mu = 0$  and  $\nu = 0.3$  eV.

which leads to  $\gamma_{MX} = -\gamma_{XM}$ . Therefore the Berry phase of two boundary states vanish at on-site energy  $\mu = 0$ .

Although these edge-band Berry phases are obtained for  $\mu = 0$ , their symmetric behavior is expected to hold even when the inversion symmetry is broken by a nonzero  $\mu$ , unless a topological phase transition occurs for one of the two edge bands. However, one of the two edge-band Berry phases may be ill-defined when the amplitude of  $\mu$  increases, since the corresponding edge band may partially merge into the valence bulk bands [e.g. see Fig. 2(b) and (c) in the main text]. Therefore we have only considered the multi-band Berry phase  $\gamma$  in the main text.

## Appendix B: Corner states of armchair boundaries

In this appendix we discussed AB-stacked TMDs with square structure, which host both armchair and zigzag edges. Taking into account two types of M-X and X-M zigzag edges, we obtain four types of different nanoflakes, namely type-A and type-B denoted in Fig. 10(a), with either an even or an odd  $N_y$ , the number of M atoms along  $y$  direction. Their corresponding symmetries are indicated in Table II.

As seen in Fig. 10(b) and (c), a type-A square lattice with an odd  $N_y$  has four degenerate corner states, distributing evenly on the four corners. This is because it is the most symmetric case in the four types of square lattices, satisfying both the inversion symmetry  $\hat{I}$  and

TABLE II. Symmetry table for different types of AB-stacked bilayer TMDs with square structure.  $N_y$  is the number of M atoms along  $y$ -direction.

	Type A	Type B
$N_y$ is odd ( $N_y > 1$ )	$\{\hat{E}, \hat{M}_x, \hat{I}, \hat{M}'_y\}$	$\{\hat{E}, \hat{M}'_y\}$
$N_y$ is even	$\{\hat{E}, \hat{M}_x\}$	$\{\hat{E}, \hat{I}\}$

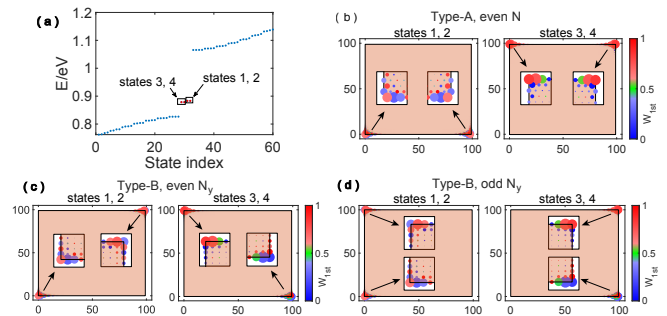


FIG. 11. Spectrum and corner states for different types of square lattices. (a) 60 Eigenenergies close to  $E = 0.95$  eV at  $\mu = 0$  for the type-A square lattice with an even  $N_y$ , with two sets of two-fold degenerate corner states (red) within the energy gap. Spectra for type-B square lattices (for both even and odd  $N_y$ ) are qualitatively the same as (a). (b) to (d) distribution of the the degenerate corner states for type-A with even  $N_y$  ( $N_x = 100, N_y = 100$ ), type-B with even  $N_y$  ( $N_x = 100, N_y = 100$ ), and type-B with odd  $N_y$  ( $N_x = 100, N_y = 101$ ), respectively. The size of each point is proportional to the summed distribution  $\rho_i$  at site  $i$ , and the colormap displays  $W_i^{1st}$ , the weight of the first-layer occupation on each site. Other parameters are  $\mu = 0$  and  $\nu = 0.3$  eV.

mirror symmetries  $\hat{M}_{x,y}$ . On the other hand, the rest three types of square lattices are less symmetric, and the corner states split into two sets of two-fold degenerate pair, as demonstrated in Fig. 11(a) for the example of a type-A square lattice with an even  $N_y$ . Their spatial distributions are illustrated in Fig. 11(b) to (d), which reflects the  $\hat{M}_x$ ,  $\hat{I}$ , and  $\hat{M}'_y$  symmetries of the corresponding square structures respectively.

In Fig. 12(a), we demonstrate the energy spectrum as a function of  $\mu$ , for type-A square lattice with odd  $N_y$ , namely with both X-M and M-X zigzag edges. Each state is marked by a quantity  $Q$  defined to distinguish armchair and zigzag edge states,

$$Q = (\text{IPR})^{\frac{4}{5}} \cdot (\text{IPR}_x)^{\frac{1}{5}},$$

$$\text{IPR} = \sum_i \left[ \sum_{\alpha} (|\psi_{i,\alpha}^{1st}|^2 + |\psi_{i,\alpha}^{2nd}|^2) \right]^2, \quad (\text{B1})$$

$$\text{IPR}_y = \sum_{i_y} \left[ \sum_{\alpha, i_x} (|\psi_{i,\alpha}^{1st}|^2 + |\psi_{i,\alpha}^{2nd}|^2) \right]^2,$$

where the site index  $i$  is further expressed as  $(i_x, i_y)$  to



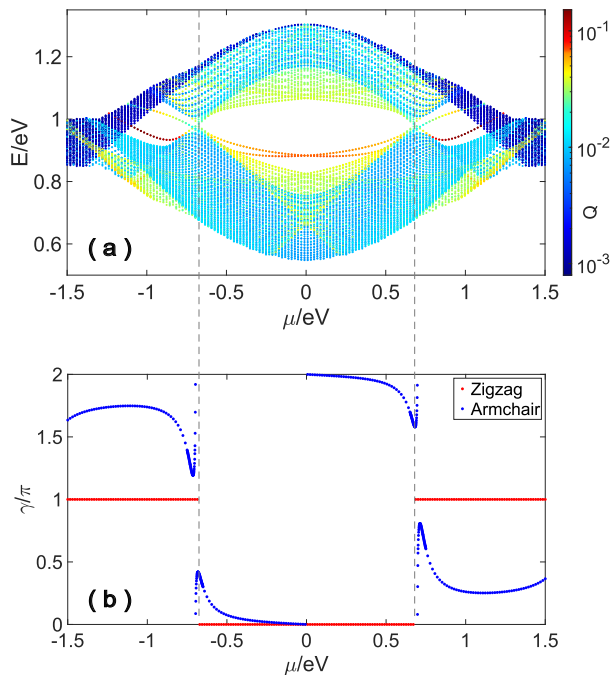


FIG. 12. (a) Eigenenergy versus on-site energy in AB-stacked bilayer TMDs with Type-A structure and odd  $N_y$ . 200 points around 0.92 eV are taken. The size of the lattice  $N_x = 71$ ,  $N_y = 71$ . The interlayer coupling strength is chosen to be  $\nu = 0.3$  eV. (b) Multiband Berry phases for all eigenstates below the edge gap, for zigzag (red) and armchair (blue) nanoribbons respectively.

indicate different positions along  $x$  and  $y$  directions, and  $\text{IPR}_y$  describes the localization strength along  $y$  direction. With this definition, perfectly localized zigzag and armchair edge states are expected to have  $Q \approx (1/N_x)^{4/5}$  and  $1/N_y$ , as they are localized along  $y$  and  $x$  directions, respectively.

As shown in the figure, the four-fold degenerate corner states split into two pairs of two-fold degenerate ones, due to the breaking of inversion symmetry under a nonzero  $\mu$ . The gap of both zigzag and armchair edge states is seen closes at  $|\mu| \approx 0.67$  eV, the same as for the cases with zigzag edges only. As discussed in the main text, the gap closing and reopening represents a topological phase transition that trivializes one of the M-X and X-M zigzag edges, thus only one pair of edge states can be attributed to zigzag edges when  $|\mu| \gtrsim 0.67$  eV. However, the gap closing and reopening also indicate a band inversion for the armchair edge bands, which are gapped at  $\mu = 0$ . Thus we still observe two pairs of edge states after the transition, with one of them originating from an armchair-edge band inversion.

In Fig. 12(b), we display the Berry phases of both zigzag and armchair nanoribbons, where the later is found to be not quantized generally. Nevertheless, the armchair Berry phase is found to be 0 at  $\mu = 0$ , indicating that the armchair edges are topologically trivial when  $\mu$  is small, i.e. within the parameter region between the two gap closing points for armchair edge states. The rapid change of the armchair Berry phase at the gap closing points hints a transition analogous to a topological one, which reflects the origin of armchair-edge band inversion for one pair of edge states at  $|\mu| \gtrsim 0.67$  eV.

\* lilh56@mail.sysu.edu.cn

- <sup>1</sup> M Zahid Hasan and Charles L Kane, “Colloquium: topological insulators,” *Reviews of modern physics* **82**, 3045 (2010).
- <sup>2</sup> Xiao-Liang Qi and Shou-Cheng Zhang, “Topological insulators and superconductors,” *Reviews of Modern Physics* **83**, 1057 (2011).
- <sup>3</sup> Wladimir A. Benalcazar, B. Andrei Bernevig, and Taylor L. Hughes, “Electric multipole moments, topological multipole moment pumping, and chiral hinge states in crystalline insulators,” *Physical Review B* **96**, 245115 (2017).
- <sup>4</sup> Wladimir A. Benalcazar, B. Andrei Bernevig, and Taylor L. Hughes, “Quantized electric multipole insulators,” *Science* **357**, 61–66 (2017).
- <sup>5</sup> Frank Schindler, Ashley M Cook, Maia G Vergniory, Zhijun Wang, Stuart S P Parkin, B Andrei Bernevig, and Titus Neupert, “Higher-order topological insulators,” *SCIENCE ADVANCES* (2018).
- <sup>6</sup> Frank Schindler, Zhijun Wang, Maia G. Vergniory, Ashley M. Cook, Anil Murani, Shamashis Sengupta, Alik Yu. Kasumov, Richard Deblock, Sangjun Jeon, Ilya Drozdov, H el ene Bouchiat, Sophie Gu eron, Ali Yazdani, B. Andrei Bernevig, and Titus Neupert, “Higher-order topology in bismuth,” *Nature Physics* **14**, 918–924 (2018).

- <sup>7</sup> Moon Jip Park, Youngkuk Kim, Gil Young Cho, and SungBin Lee, “Higher-Order Topological Insulator in Twisted Bilayer Graphene,” *Physical Review Letters* **123**, 216803 (2019).
- <sup>8</sup> Yuan Fang and Jennifer Cano, “Higher-order topological insulators in antiperovskites,” *Physical Review B* **101**, 245110 (2020).
- <sup>9</sup> Adhip Agarwala, Vladimir Juri ci c, and Bitan Roy, “Higher-order topological insulators in amorphous solids,” *Physical Review Research* **2**, 012067 (2020).
- <sup>10</sup> Bi-Ye Xie, Guang-Xu Su, Hong-Fei Wang, Hai Su, Xiao-Peng Shen, Peng Zhan, Ming-Hui Lu, Zhen-Lin Wang, and Yan-Feng Chen, “Visualization of Higher-Order Topological Insulating Phases in Two-Dimensional Dielectric Photonic Crystals,” *Physical Review Letters* **122**, 233903 (2019).
- <sup>11</sup> Qiang Wei, Xuewei Zhang, Weiyin Deng, Jiuyang Lu, Xueqin Huang, Mou Yan, Gang Chen, Zhengyou Liu, and Suotang Jia, “Higher-order topological semimetal in acoustic crystals,” *Nature Materials* **20**, 812–817 (2021).
- <sup>12</sup> Haoran Xue, Yahui Yang, Fei Gao, Yidong Chong, and Baile Zhang, “Acoustic higher-order topological insulator on a kagome lattice,” *Nature Materials* **18**, 108–112 (2019).
- <sup>13</sup> Xiang Ni, Matthew Weiner, Andrea Al u, and Alexander B. Khanikaev, “Observation of higher-order topological

- acoustic states protected by generalized chiral symmetry,” *Nature Materials* **18**, 113–120 (2019).
- 14 Zhang-Zhao Yang, Xin Li, Yao-Yin Peng, Xin-Ye Zou, and Jian-Chun Cheng, “Helical Higher-Order Topological States in an Acoustic Crystalline Insulator,” *Physical Review Letters* **125**, 255502 (2020).
  - 15 Haiyan Fan, Baizhan Xia, Liang Tong, Shengjie Zheng, and Dejie Yu, “Elastic Higher-Order Topological Insulator with Topologically Protected Corner States,” *Physical Review Letters* **122**, 204301 (2019).
  - 16 Biye Xie, Hai-Xiao Wang, Xiujuan Zhang, Peng Zhan, Jian-Hua Jiang, Minghui Lu, and Yanfeng Chen, “Higher-order band topology,” *Nature Reviews Physics* **3**, 520–532 (2021).
  - 17 B Andrei Bernevig, Claudia Felser, and Haim Beidenkopf, “Progress and prospects in magnetic topological materials,” *Nature* **603**, 41–51 (2022).
  - 18 Benjamin J Wieder, Barry Bradlyn, Jennifer Cano, Zhijun Wang, Maia G Vergniory, Luis Elcoro, Alexey A Soluyanov, Claudia Felser, Titus Neupert, Nicolas Regnault, *et al.*, “Topological materials discovery from crystal symmetry,” *Nature Reviews Materials* **7**, 196–216 (2022).
  - 19 Habib Rostami, Reza Asgari, and Francisco Guinea, “Edge modes in zigzag and armchair ribbons of monolayer MoS<sub>2</sub>,” *Journal of Physics: Condensed Matter* **28**, 495001 (2016).
  - 20 Zhijun Wang, Benjamin J. Wieder, Jian Li, Binghai Yan, and B. Andrei Bernevig, “Higher-order topology, monopole nodal lines, and the origin of large fermi arcs in transition metal dichalcogenides  $xte_2$  ( $x = \text{Mo}, \text{W}$ ),” *Phys. Rev. Lett.* **123**, 186401 (2019).
  - 21 Jiang Zeng, Haiwen Liu, Hua Jiang, Qing-Feng Sun, and X. C. Xie, “Multiorbital model reveals a second-order topological insulator in 1 H transition metal dichalcogenides,” *Physical Review B* **104**, L161108 (2021).
  - 22 Shifeng Qian, Gui-Bin Liu, Cheng-Cheng Liu, and Yugui Yao, “C<sub>n</sub>-symmetric higher-order topological crystalline insulators in atomically thin transition metal dichalcogenides,” *Physical Review B* **105**, 045417 (2022).
  - 23 Jun Jung and Yong-Hyun Kim, “Hidden breathing kagome topology in hexagonal transition metal dichalcogenides,” *Physical Review B* **105**, 085138 (2022).
  - 24 Marcio Costa, Bruno Focassio, Luis M. Canonico, Tarik P. Cysne, Gabriel R. Schleder, R. B. Muniz, Adalberto Fazzio, and Tatiana G. Rappoport, “Connecting higher-order topology with the orbital hall effect in monolayers of transition metal dichalcogenides,” *Phys. Rev. Lett.* **130**, 116204 (2023).
  - 25 Gui-Bin Liu, Wen-Yu Shan, Yugui Yao, Wang Yao, and Di Xiao, “Three-band tight-binding model for monolayers of group-VIB transition metal dichalcogenides,” *Physical Review B* **88**, 085433 (2013).
  - 26 Haining Pan, Ming Xie, Fengcheng Wu, and Sankar Das Sarma, “Topological phases in ab-stacked  $\text{mote}_2/\text{wse}_2$ :  $F_2$  topological insulators, chern insulators, and topological charge density waves,” *Phys. Rev. Lett.* **129**, 056804 (2022).
  - 27 Max Geier, Luka Trifunovic, Max Hoskam, and Piet W Brouwer, “Second-order topological insulators and superconductors with an order-two crystalline symmetry,” *Physical Review B* **97**, 205135 (2018).
  - 28 Luka Trifunovic and Piet W Brouwer, “Higher-order bulk-boundary correspondence for topological crystalline phases,” *Physical Review X* **9**, 011012 (2019).
  - 29 Motohiko Ezawa, “Edge-corner correspondence: Boundary-obstructed topological phases with chiral symmetry,” *Physical Review B* **102**, 121405 (2020).
  - 30 Koichi Asaga and Takahiro Fukui, “Boundary-obstructed topological phases of a massive dirac fermion in a magnetic field,” *Physical Review B* **102**, 155102 (2020).
  - 31 Xianxin Wu, Wladimir A Benalcazar, Yinxiang Li, Ronny Thomale, Chao-Xing Liu, and Jiangping Hu, “Boundary-obstructed topological high- $T_c$  superconductivity in iron pnictides,” *Physical Review X* **10**, 041014 (2020).
  - 32 Apoorv Tiwari, Ammar Jahin, and Yuxuan Wang, “Chiral dirac superconductors: Second-order and boundary-obstructed topology,” *Physical Review Research* **2**, 043300 (2020).
  - 33 Eslam Khalaf, Wladimir A. Benalcazar, Taylor L. Hughes, and Raquel Queiroz, “Boundary-obstructed topological phases,” *Physical Review Research* **3**, 013239 (2021).
  - 34 Linhu Li, Muhammad Umer, and Jiangbin Gong, “Direct prediction of corner state configurations from edge winding numbers in two- and three-dimensional chiral-symmetric lattice systems,” *Physical Review B* **98**, 205422 (2018).
  - 35 Linhu Li, Weiwei Zhu, and Jiangbin Gong, “Direct dynamical characterization of higher-order topological phases with nested band inversion surfaces,” *Science Bulletin* **66**, 1502–1510 (2021).
  - 36 Zhoutao Lei, Yuangang Deng, and Linhu Li, “Topological classification of higher-order topological phases with nested band inversion surfaces,” *Phys. Rev. B* **106**, 245105 (2022).
  - 37 Linhu Li, Eduardo V. Castro, and Pedro D. Sacramento, “Strain-induced topological phase transition at zigzag edges of monolayer transition-metal dichalcogenides,” *Physical Review B* **94**, 195419 (2016).
  - 38 T. Čadež, L. Li, E. V. Castro, and J. M. P. Carmelo, “Robust one dimensionality at twin grain boundaries in MoSe<sub>2</sub>,” *Physical Review B* **99**, 155109 (2019).
  - 39 Francisco MO Brito, Linhu Li, João MVP Lopes, and Eduardo V Castro, “Edge magnetism in transition metal dichalcogenide nanoribbons: Mean field theory and determinant quantum monte carlo,” *Physical Review B* **105**, 195130 (2022).
  - 40 Ashwin Ramasubramaniam, Doron Naveh, and Elias Towe, “Tunable band gaps in bilayer transition-metal dichalcogenides,” *Phys. Rev. B* **84**, 205325 (2011).
  - 41 Ashok Kumar and PK Ahluwalia, “Semiconductor to metal transition in bilayer transition metals dichalcogenides  $\text{mx}_2$  ( $\text{m} = \text{mo}, \text{w}$ ;  $\text{x} = \text{s}, \text{se}, \text{te}$ ),” *Modelling and Simulation in Materials Science and Engineering* **21**, 065015 (2013).
  - 42 J. C. Slater and G. F. Koster, “Simplified LCAO Method for the Periodic Potential Problem,” *Physical Review* **94**, 1498–1524 (1954).
  - 43 H. H. Jaffé, “Some Overlap Integrals Involving  $d$  Orbitals,” *The Journal of Chemical Physics* **21**, 258–263 (1953).
  - 44 Joe L. Roberts and H. H. Jaffé, “Some Overlap Integrals Involving  $d$  Orbitals. II,” *The Journal of Chemical Physics* **27**, 883–886 (1957).